REPORT DOCUMENTATION PAGE

Form Approved
OMB No. 0704-0188

1. REPORT DATE *(DD-MM-YYYY)*	2. REPORT TYPE	3. DATES COVERED *(From - To)*
07/31/2017	Final	4/1/2016 - 5/31/2017

4. TITLE AND SUBTITLE
Understanding and Prevention of Transient Voltages and Dielectric Breakdown in High Voltage Battery Systems

5a. CONTRACT NUMBER

5b. GRANT NUMBER
N00014-16-1-2453

5c. PROGRAM ELEMENT NUMBER

6. AUTHOR(S)
David Wetz, PhD

5d. PROJECT NUMBER

5e. TASK NUMBER

5f. WORK UNIT NUMBER

7. PERFORMING ORGANIZATION NAME(S) AND ADDRESS(ES)
University of Texas at Arlingon
416 Yates Street, Rm. 537
Arlington, Texas, 76019

8. PERFORMING ORGANIZATION REPORT NUMBER

9. SPONSORING/MONITORING AGENCY NAME(S) AND ADDRESS(ES)
Office of Naval Research
875 N Randolph Street
Arlington, VA, 22203-1995

10. SPONSOR/MONITOR'S ACRONYM(S)
ONR

11. SPONSOR/MONITOR'S REPORT NUMBER(S)

12. DISTRIBUTION/AVAILABILITY STATEMENT
Distribution A

13. SUPPLEMENTARY NOTES

14. ABSTRACT
This work is aimed at studying how transients are generated in high current battery systems and how vented Li-ion electrolyte gas impacts the dielectric breakdown strength of ambient air.

15. SUBJECT TERMS
Energy storage, dielectric breakdown, pulsed power

16. SECURITY CLASSIFICATION OF:			17. LIMITATION OF ABSTRACT	18. NUMBER OF PAGES	19a. NAME OF RESPONSIBLE PERSON
a. REPORT	b. ABSTRACT	c. THIS PAGE			David Wetz
					19b. TELEPHONE NUMBER *(Include area code)*
U	U	U	None	35	8172720719

Final Report

Understanding and Prevention of Transient Voltages and Dielectric Breakdown in High Voltage Battery Systems

Submitted to:

Mr. Donald Hoffman
donald.hoffman@navy.mil

Grant Number N00014-16-1-2453

Performance Period: April 1, 2016 – May 31, 2017

Submitted by:
David Alan Wetz Jr., PhD (PI)
Associate Professor
Electrical Engineering Dept.
University of Texas at Arlington
College of Engineering
416 Yates Street, Rm. 518
Arlington, Texas 76019-0016
Phone: (817) 272-1058

Introduction

The future fleet of U.S. Navy vessels may be deployed with a number of high power electrical loads that operate transiently. The transient nature of the loads will impart high stress on the traditional shipboard power system, possibly pushing it outside of the acceptable power quality standards. To restore power quality and increase system reliability, it is being proposed that electrochemical energy storage systems be used as a buffer. The proposed energy storage systems will store a great deal of energy and could be designed with open circuit potentials (OCPs) as high as 1 kV. Since size and weight aboard the vessel is limited, the batteries need to be designed as compactly as possible. These energy storage systems will likely be in a different area of the vessel than the loads they provide power to. Long cables will be used to connect busses that provide power to different loads introducing inductance to the system based on the length and diameter of those cables. High power electrical loads combined with the inductance introduced can lead to voltage transients well over the energy storage systems OCP, possibly leading severe damage to system components. Another issue is that in the event of a battery failure, in which one or more cells are compromised, organic electrolyte may be vented within the air dielectric separating points of higher and lower potential. How the vented electrolyte impacts the dielectric strength of the surrounding environment is of concern, especially given the battery's high operational voltage, its compact construction, and the high energy it stores. The study documented here is split into two tasks. The first is first aimed at studying methods to mitigate voltage transients and although this study does not use a system with an OCP of 1 kV, the data gathered is helpful in identifying effective suppression techniques. The second investigates the dielectric strength of the vented electrolyte from a lithium-iron-phosphate (LFP) battery when exposed to potentials representative of a future shipboard energy storage system.

Task 1: Investigate Methods to Mitigate Voltage Transients

I. Introduction

In future naval ships, there will be several unique high power loads which will be operated in both continuous and pulsed modes of operation [1,2]. When high pulsed power loads are sourced, they drag down their source's DC or AC bus voltage considerably, heavily impacting the power quality. While generators alone can likely be sized properly to account for large transient loads, they will be much larger than they really need to be taking up valuable space aboard a ship that is desperately needed for other things. With this in mind, DC and AC sources can be integrated into unique power system architectures that employ energy generation and storage capable of working together to supply the intermittent loads. The use of energy storage to buffer the generation minimized variations in generator output power allowing its power quality to be maintained [3-6]. Power system architectures which combine both electrochemical batteries, capacitors, and the standard AC generation are preferred [5-6]. This leads to both DC and AC buses existing in the architecture, requiring active power conversion between DC and AC sources. This is not a new challenge, as it is one faced every day as power systems engineers try to integrate batteries, solar panels, and wind turbines onto the already existing electrical grid, either in homes or in the distribution network, but the loads being sourced in those applications are vastly different than those being sourced by a future naval ship and therefore special attention and research is needed to understand how to overcome these challenges.

Once integrated into a combined power system, the energy storage will supply pulsed high currents to transiently operated loads. As it would be optimal to locate the energy storage very close to the load, it is almost always impossible to do so. As a result long cables will be used to carry current from the energy storage to the load. Long cables of course translates into high equivalent series resistances and inductances being placed in series with the energy storage and the load. The high slew rate of the loads of interest coupled with the high currents being carried will result in high inductive voltage spikes being induced on the transmission system. A similar phenomena will be observed in the event of a high current protective fuse opening. The spikes are induced according to equation 1. While this problem is challenging enough to overcome, it is proposed that energy storage systems be implemented with open circuit potentials (OCP) in excess of 1 kV. High voltage spikes induced on top of this already high OCP can result in dangerously high voltage transients occurring that can easily punch through electrical insulation. If this occurs, it can result in the formation of short circuits that bypass safety devices and quickly deplete the batteries at high current rates. These are events that could have very serious consequences and therefore proper understanding of how to mitigate them is needed.

$$V_S = L \times \frac{di}{dt} \ (V) \tag{1}$$

In 2015, experiments were conducted using a current profile containing abrupt changes to simulate a specified load profile. While conducting these experiments it became clear the severity of these voltage transients were greater than expected. The transients encountered caused the programmable loads to shut down and ultimately halted the experiment. The experiment was first conducted using a 20S/1P module of 30 Ah lithium-ion batteries evaluated under the current profile seen in the left side of Figure 1. Notice in the profile the abrupt changes in current which are the cause of the voltage transients produced. To the right of the transient profile is a photograph of the bus work connecting the battery to the programmable load. The current profile is comprised of three short discharges of 300 A, followed by a short recharge of 750 A

to return the energy drained from the module. When attempting the experiment using the 20S/1P module transients as higher than 113 V were observed. Keep in mind that the OCP of the battery is only 76V. The Chroma programmable loads have a maximum rated voltage of 80 V, but contain their own internal transient protection once 113 V is reached. To better understand the problem at hand, a 10S/1P battery was experimentally studied. In those experiments, transients were observed with peak voltages just under 90 V which allowed the load to remain operational. Figure 2 zooms in on one of the voltage transient profiles measured from a 10S/1P battery when it was evaluated using the current profile from Figure 1. Keep in mind that in this case the OCP of the module used is only 38 V. Voltage transients such as these are extremely concerning considering the voltage spike produced is over twice the OCP of the module. If similar scale transients were to occur on 1 kV battery, they could exceed 2 kV and would be extremely dangerous to equipment and personnel. This prompted the investigation performed here that is aimed at evaluating different methods of voltage transient to study their effectiveness. In this particular study three different voltage transient suppression techniques have been evaluated. These include transient voltage suppression (TVS) diodes, metal oxide varistors (MOV's), and an active voltage suppression circuit respectively.

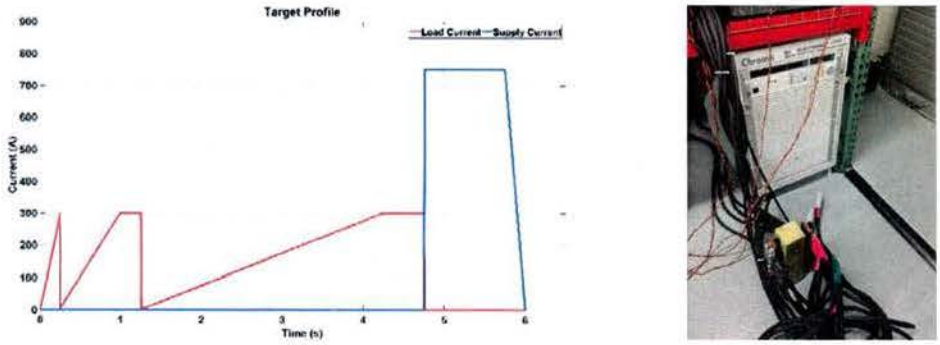

Figure 1: Current profile (left) experimentally evaluated using a 20S/1P module of lithium-ion batteries. Photograph of the cables connecting the source to the load (right)

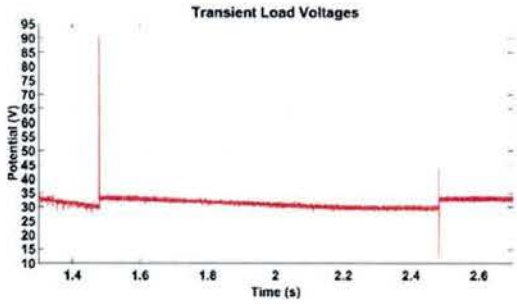

Figure 2: Transient voltage spikes measured when the current profile shown in Figure 1 were executed using the 20S/1P module.

II. Methods of Transient Suppression

II.a. TVS Diodes

The first type of suppression to be discussed are TVS diodes, which are solid state P-N junction devices designed to protect sensitive semiconductors from the damaging effects of transient voltages. A TVS diode's electrical characteristics are primarily based on factors such as junction area, doping concentration,

and substrate resistivity [9]. If the voltage exceeds the clamping voltage of the TVS diode, current flows through the diode causing the voltage clamp. The clamping voltage is adjusted by varying the carrier doping levels within the diode. The V-I relationship for both unidirectional and bidirectional TVS diodes is seen in Figure 3. TVS diodes are known for having fast switch on times but their switch off times are slightly slower and can result in extra power to be dissipated through the diode. TVS diodes performance is not significantly degraded with lifetime and the number of transients applied, as long as the TVS is properly sized. It is important to note that TVS diodes do act as near short circuits when they fail but mostly only fail due to thermal stress when used in a situation they are not specified for, therefore a fuse is recommended for additional safety.

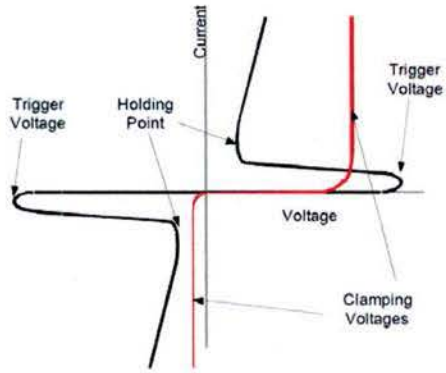

Figures 3: V-I relationship of a TVS diode. Red curve represents unidirectional TVS and the black curve represents bidirectional TVS.

TVS diodes are offered at discretely incremented clamping voltages by most manufacturers. This is a bit of a problem if the voltages offered do not line up perfectly with the users intended application. Often a 'next best' solution must be adopted resulting in the allowance of transients that are slightly higher than desired. In many cases this is not problematic but it will of course stack up if multiple devices must be combined in series for example. More about this will be discussed later.

II.b. Metal Oxide Varistors

The second method to be discussed are known as MOVs that are essentially variable resistors with a non-linear *i-v* curve, Figure 4. Their body structure consists of ZnO grains separated by grain boundaries which provide P-N junction characteristics. These boundaries are responsible for blocking conduction up to a certain voltage and are the source of the nonlinear electrical conduction at higher voltages [10].

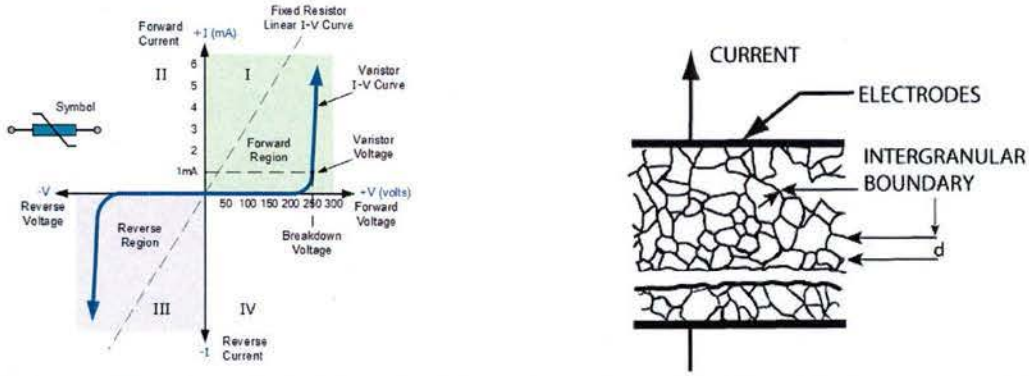

Figure 4: Symmetrical non-linear V-I relationship (left) microstructure of an MOV showing grains of ZnO of average size d separated by intergranular boundaries (right) [10].

Varistors tend to be able to dissipate more power at a smaller form factor and at a lower cost than TVS diodes however unlike TVS diodes, their degradation is inversely proportional to the volume of the device. The data sheet for a specific device typically provides an approximate number of surges it can handle before failing. MOVs can fail as either an open or a short circuit depending on multiple factors, such as disk diameter for example, and can result in the device exploding or catching fire as shown in Figure 5 [11].

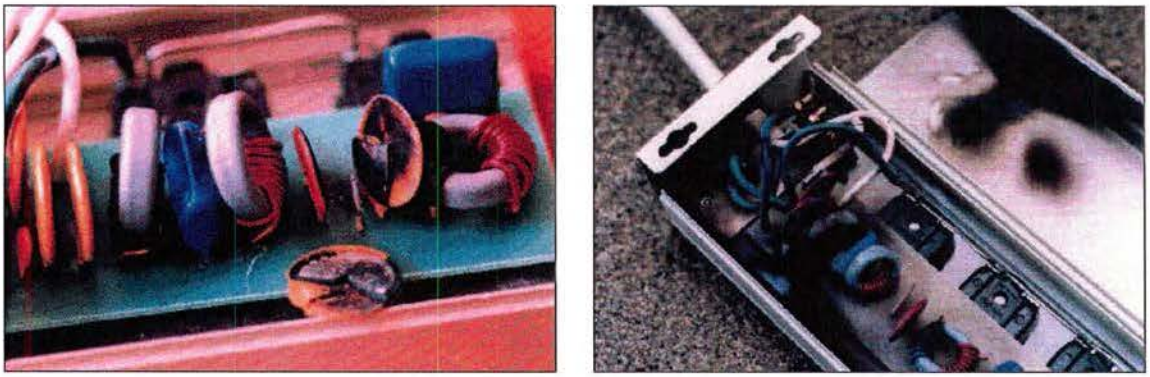

Figure 5: MOV surge protection is lost (left) example of dangerous construction, where failed MOV, packed too tightly between adjacent components and cannot split open (right) [11].

II.c. Active Suppression Technologies

The third method of voltage transient suppression explored in this work is an active design utilizing electronic components. The above mentioned methods of suppression use discrete components whereas with an active suppression design the voltage transient is suppressed using active components, such as logic ICs and MOSFETs. Active clamping brings some advantages including the ability to be adjusted by the user to meet dynamically changing requirements. A disadvantage they have is that they often have switching characteristics that are also transient in nature and therefore lack the same sort of nonlinear *i-v* curve that the TVS and MOV technologies offer. In the work performed here, a few different active topologies have been studied with limited success.

III. Experimental Setup

The experimental setup is similar to the one used in 2015 with the only difference being the type of battery that is utilized. In 2015, a 10S/1P battery made up of Saft VL30AFe cells was used. In the work performed here, the battery module, shown in Figure 6, consists of a 10S/1P array of GAIA 20 Ah LFP, lithium iron phosphate, cells contained within an aluminum cooling module. An ACTIA® battery management system (BMS), is also used.

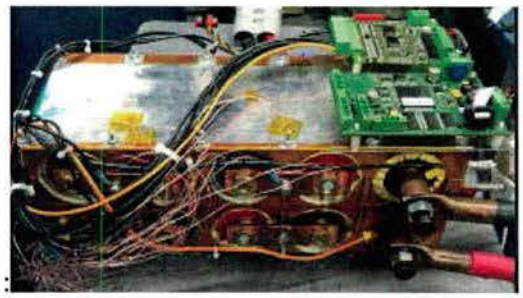

Figure 6: The GAIA cell module in a 10S/1P configuration with BMS board attached.

The GAIA cells have a nominal voltage of 3.2 V, a max voltage of 3.8 V, and an approximate ESR of 1.3 mΩ. They have a rated peak continuous current as high as 500 A and are recommended not to exceed a temperature of 65°C. In this configuration, the nominal pack voltage is approximately 32 V and should not exceed 38 V. The transient profile is generated by a NI-USB-6211 multifunction IO device that supplies analog signals to a Chroma model 63209 programmable load and two Chroma model 62050P power supplies, all of which can be seen below in Figure 7.

Figure 7: The NI-USB-6211 multifunction IO device used to control the load and supplies (left) the Chroma load used for discharge current (middle) one of the two Chroma supplies used for the charge current (right).

The Chroma load is used in the available 1000A/80V/15.6kW range. The Chroma power supplies used configured in a master-slave setup and are each capable of 100V/100A/5kW. The current profile used is very similar to the profile of interest used in the 2015 experiment with the only difference being that the charge current is limited to 180 A. The supplies and load are connected to common buss block and then from the buss block to the GAIA module using 3/0 gauge welding cable. These cables introduce inductance to the system based off of the cables length and diameter. The formula for calculating the inductance can be see below in equation 2.

$$L = 2l\left(ln\left(\left(\frac{2l}{d}\right)\left(1\sqrt{1+\left(\frac{d}{2l}\right)^2}\right)\right) - \sqrt{1+\left(\frac{d}{2l}\right)^2} + \frac{\mu}{4} + \left(\frac{d}{2l}\right)\right) \quad (2)$$

Using equation 2, the inductance can be calculated for a certain length of cable used assuming the diameter of 3/0 gauge cable as 0.229 inches. This experiment expresses interest in how a change in inductance affects the transients induced and the effectiveness of the different suppression techniques. With that, two different lengths of cable have been used and data has been collected from each. Prior to experimentation, models were developed and run using LTSpice. TVS and MOV models are supplied by the manufacturers and then imported into the model. The battery module is modeled as a very large capacitor with a designated initial voltage and a series resistance. The capacitance of the module is estimated at roughly 50,000 F and the series resistance of the battery and the cables is approximately 38 mΩ. As previously mentioned, the cables introduce inductance to the system and therefore will be modeled using non ideal inductors. The two cable lengths used are 465 cm and 584 cm respectively. Using equation 2 and the cable dimensions, the approximate inductance introduced by these cables is 6.8 μH and 8.82 μH respectively. In order to induce a voltage transient, a MOSFET is used with a pulsed voltage source attached to its gate that will act as a switch in the circuit, simulating the fast changes in current in the profile of interest. The simulation is run for 50 ms and the initial condition of the battery is set at 33 V, the nominal voltage of the module. The model is shown in Figure 8 along with a photograph of the experimental setup. The rise time and fall time on the voltage source are set to closely match that of the supplies and load. The schematic is the same for both lengths of cable with only the inductance value changing. The voltage source driving the FET will first turn on at 10 ms and then off at 30 ms, which is where we expect to see the transients of interest. Based on equation 1 we are to expect a larger transient when the longer cables are used, introducing a larger inductance. The transient voltages obtained from simulation are shown in Figure 9 for each respective cable length. As shown, the 465 cm cable should produce a roughly 56 V transient while the 584 cm long cable is expected to produce transients of nearly 64 V. Both cables produce transients that are within the load's voltage range.

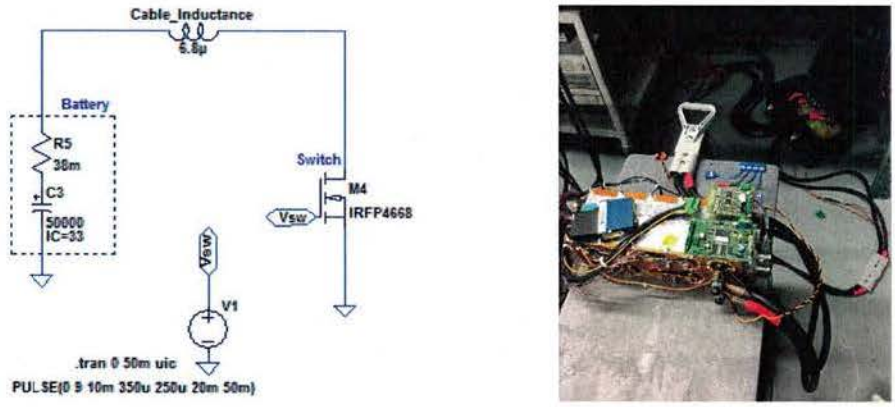

Figure 8: The schematic of the experimental setup (left) a photograph of the actual setup used in the voltage transient study including the bus, the cables, and the battery module (right).

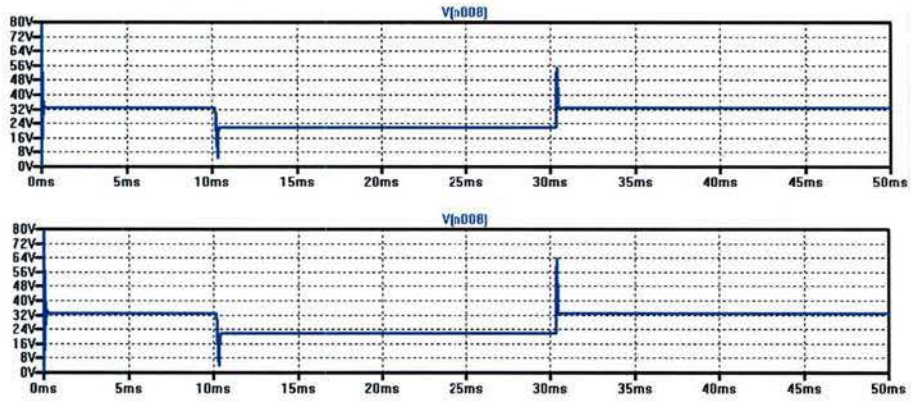

Figure 9: Output from the system modeling the use of the shorter cables with an inductance of 6.8 μH (top) and 8.82 μH cables (below).

IV. Experimental Results

Early in the experimental process, there was an effort to use the new setup to obtain transients similar to those obtained in 2015 and to validate the simulation results shown in Figure 9. The load and supplies were controlled by the NI-USB-6211 multifunction IO device, which uses a USB input to control output voltages using a LabVIEW program. The LabVIEW program controls the NI device that delivers an analog signal to the load and supplies corresponding to the desired scaled output. Each of the two cable lengths were evaluated three times for repeatability. Figure 10 shows the transient voltages recorded for both lengths of cable along with the current profile.

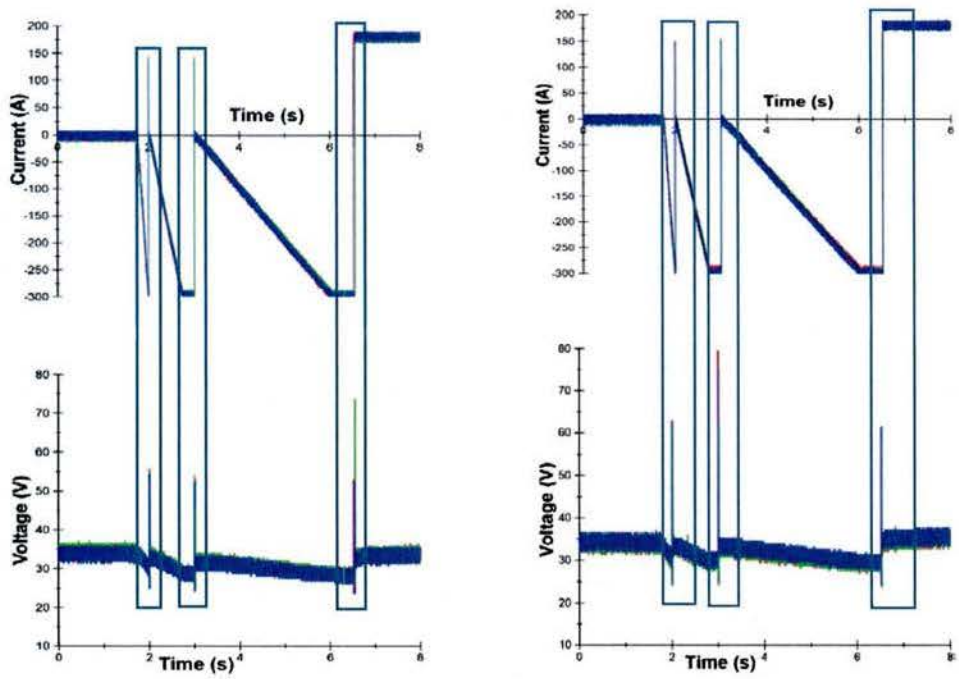

Figure 10: Current (above) and voltage (below) profiles for 465 cm cable (left) and 584 cm cable (right) respectively.

Figure 10 illustrates how the transients align with the abrupt changes in the current profile for each length of cable. The simulation results are also verified as the transient voltages obtained experimentally closely match the simulation values obtained in Figure 9. Once the simulations were proven as accurate, the next hurdle was to begin to evaluate the suppression topologies ability to prevent transients.

IV.a. TVS Diodes

TVS diodes were evaluated from Littlefuse who offers a wide selection of devices across a range of different voltage and power levels. As mentioned earlier, Littlefuse provides SPICE models on their website for many of their diodes that were used in evaluating the simulation model. Based off of the pack voltage, two TVS diodes were chosen to be evaluated in this study. One was sized for the modules nominal voltage and the other was chosen assuming the module is fully charged. Those are the 15KPA33CA and the 15KPA40CA, respectively. The electrical characteristic for the two TVS diodes are listed in Table 1 below.

Electrical Characteristics (T_A=25°C unless otherwise noted)

Part Number (Uni)	Part Number (Bi)	Reverse Stand off Voltage V_R (Volts)	Breakdown Voltage V_{BR} (Volts) @ I_T		Test Current I_T (mA)	Maximum Peak Pulse Current I_{PP} (A)	Maximum Reverse Leakage I_R @ V_R (μ A)	Maximum Clarrping Voltage V_C @ I_{PP} (V)	Agency Approval
			MIN	MAX					
→ 15KPA33A	15KPA33CA	33	36.9	40.4	5	276.1	2	54.7	X
15KPA36A	15KPA36CA	36	40.2	44.0	5	252.5	2	59.8	X
→ 15KPA40A	15KPA40CA	40	44.7	48.9	5	229.5	2	65.8	X

Table 1: The characteristics of the two tested TVS diodes, the 15KPA33CA and the 15KPA40CA.

The two TVS diodes were chosen based on three main characteristics with those being the reverse standoff voltage (V_R), maximum peak pulse current (I_{PP}), and maximum clamping voltage (V_C). The first characteristic, reverse standoff voltage, is important to ensure the TVS does not affect the driving voltage. Ideally V_R is chosen to be equal to the peak operating voltage of the circuit but the 15KPA33A is chosen to examine the suppression effects if the module charged to its nominal voltage. The second main characteristic, peak pulse current, defines the maximum current the TVS diode can handle without damaging the diode. Finally the third important characteristic is the maximum clamping voltage, which defines the peak voltage across the diode when subject to I_{PP}. The power rating for both of these devices is 15 kW which is higher than that required by the experiment but given the repetitive nature of the expected transients, it was decided that more power capability is safer.

LTSPICE simulations of the system using the 15KPA33CA and 15KPA40CA TVS diodes are shown in Figure 11. The TVS diode under test is placed in parallel with the point of common coupling among the system components. As shown in Figure 11A, the TVS diode limits the peak voltage to 48 V, as opposed to 56 V seen without the TVS diode in the circuit. This is where the drawback to TVS diodes starts to be seen. Ideally, the voltage should be clamped to only a few Volts above the nominal operating voltage however due to the *i-v* curve only starting to conduct just above the desired clamp voltage, a significant voltage is allowed to build up before the diode is fully turned on. The discrete nature of the available TVS clamping voltages introduces further deviations from the desired clamp voltage as picking one with a higher or lower clamp voltage may either allow the device to conduct even in the nominal operational range or push it even further avoe the desired clamp voltage making it tough to choose the perfect device from the limited availability. None the less, this demonstrates that TVS diodes can be used to limit transient events similar to those observed in these types of systems. At least then, the maximum transient can be sized and accommodated for within the supply, bus, and load systems, respectively.

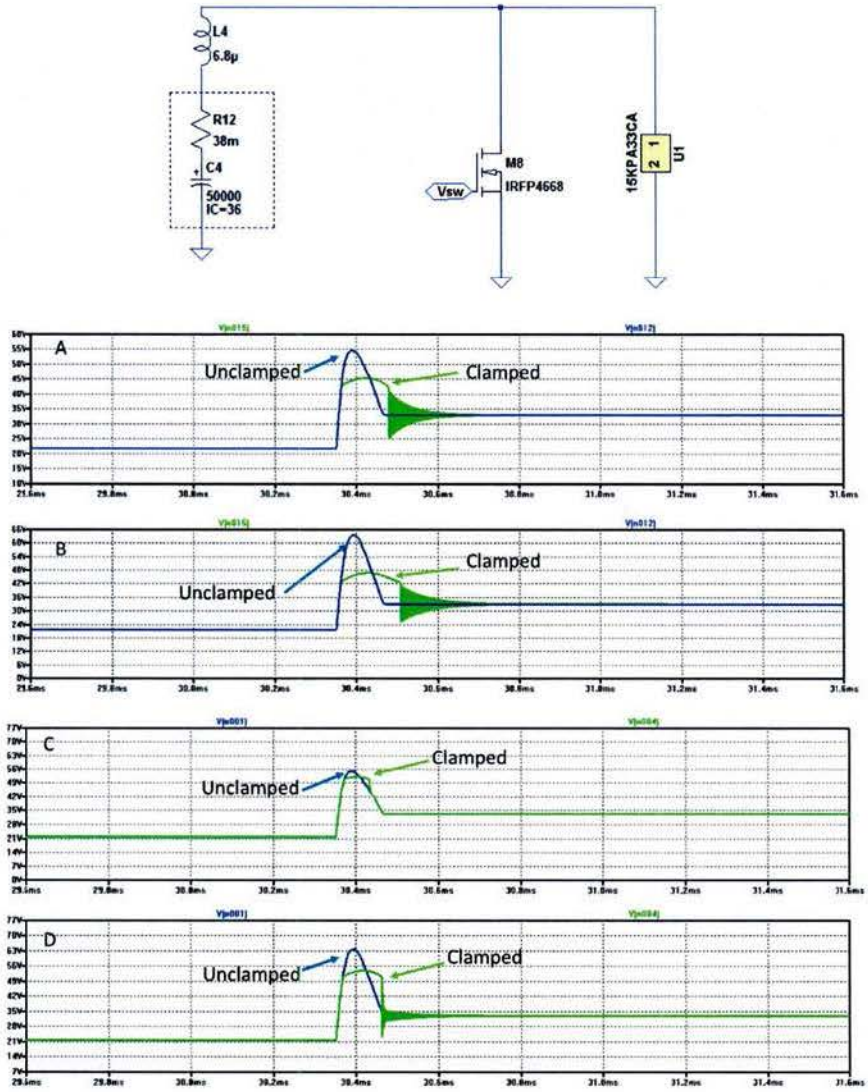

Figure 11: Simulation results of (A) 15KPA33CA using 465 cm long cable, (B) 15KPA33CA using 584 cm long cable, (C) 15KPA40CA using 465 cm long cable and (D) 15KPA40CA using 584 cm long cable.

The first TVS diode experimentally evaluated is the 15KPA33CA using the 465 cm long cable. A LeCroy WaveSurfer digital oscilloscope was to capture the transient voltage and current profiles which are captured using LeCroy differential voltage probes and a clamp-on current meter. These diagnostics are shown integrated into the setup in Figure 12.

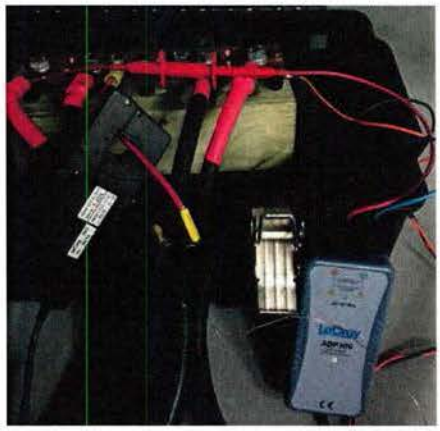

Figure 12: The system setup using the 15KPA33CA, differential voltage probes, and current meter.

Voltage and current waveforms measured during three experiments using the 15KPA33CA in place is shown in Figure 13. The transient voltage profile shows consistent transient clamping throughout all three tests at roughly 45 V, nearly 10 V less than the transients produced in the unprotected system and only 3 V less than the peak voltage the simulation suggested would be induced. The current shunted by the TVS diode is between 160 A and 175 A for the three transients. Figure 13 displays the data from only one pulsed current waveform. The next step was to evaluate how well the TVS would handle repetitive operation of the current waveform with transients occurring every few seconds for a long period of time. Prior to experimentally evaluating the repetitive operation, the energy dissipated during a single cycle was computed as shown in Figure 14 using equations 3 and 4. Knowing the energy dissipated in a single cycle, the energy dissipated in repetitive cycling could be calculated along with the expected rise in temperature.

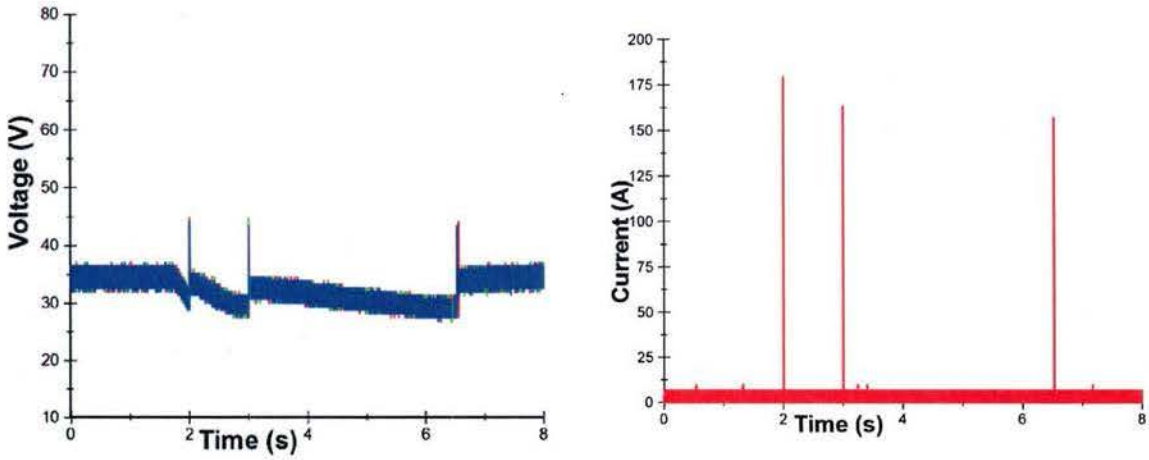

Figure 13: The transient voltage profile using the 15KPA33CA for suppression (left) the current shunted through the TVS diode (right).

$$P = V * I\ (W) \tag{3}$$

$$E = \int P * dt\ (J) \tag{4}$$

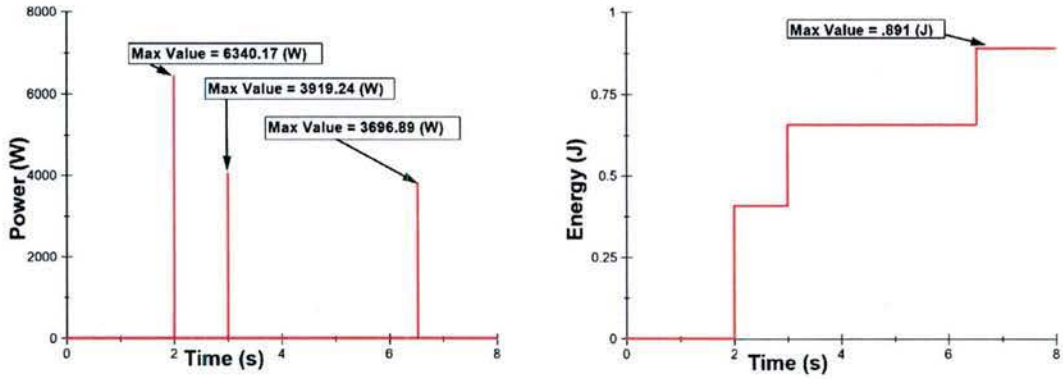

Figure 14: The power consumed by the 15KPA33CA for each voltage transient produced (left) the power consumed converted to energy of the same profile, both calculated using the equations 3 and 4 respectively (right).

As shown in Figure 14, each full cycle only dissipates roughly 0.9 J of energy. It was assumed that a continuous run consists of 60 cycles performed repetitively over roughly 10 min. The total energy dissipated by the diode is found by multiplying 0.9 J by 60, coming up with roughly 54 J. The average power is calculated by dividing the total energy dissipated by by 600 sec, which is roughly 90 mW. Referring back to the data sheet, the typical thermal resistance of junction to ambient is said to be 40 °C/W. If the average power is multiplied by the thermal constant then it is estimated that the TVS diode increases in temperature by about 3.56°C. Since the device is also cooled by the ambient air, it was determined that the diode would be able to sufficiently handle the repetitive test, the results of which are shown in Figure 15 where a T type thermocouple was used to validate the temperature rise of the diode. As shown the diodes temperature rises by roughly 3°C in each of the three experiments performed. The last two 'suppressed' transients recorded during the 60 cycle test are shown graphically in Figure 16.

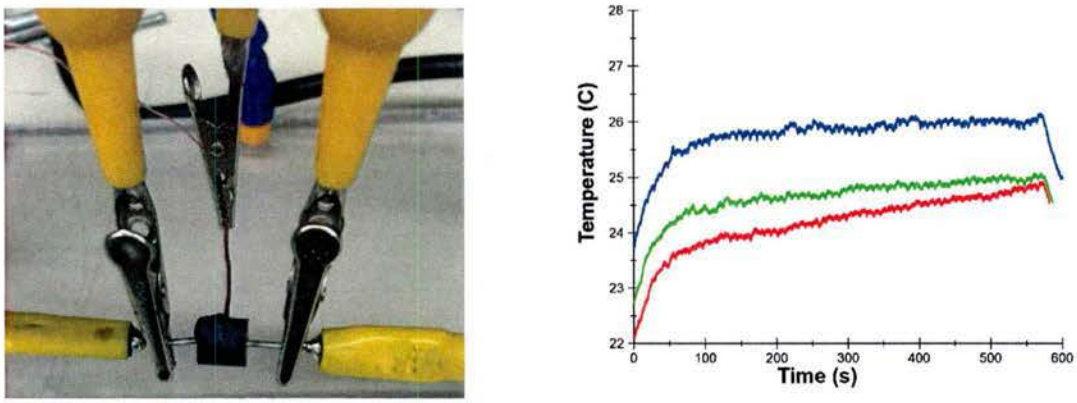

Figure 15: 15KPA33CA with a T-type thermocouple thermal epoxied to the diode for temperature measurements (left) three tests showing the temperature rise of the TVS diode during the 60 cycle tests (right).

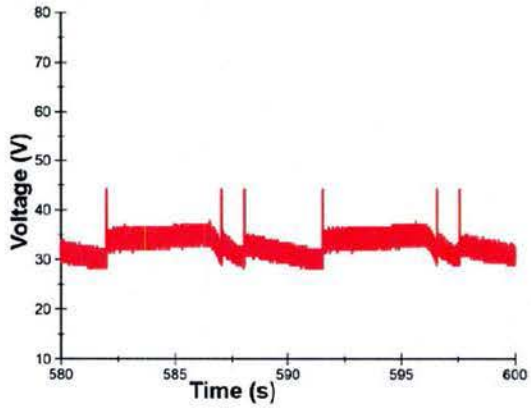

Figure 16: Transient voltage profile recorded during the last two of the 60 cycle test using the 15KPA33CA diode.

Figure 16 illustrates that the 15KPA33CA is a reliable choice for suppressing repetitive voltage transients when the module is used at its nominal voltage. As discussed earlier, TVS diodes have a very nonlinear *iv* curve and while it works well at the nominal voltage, it doesn't necessarily mean it will work at the full 38 V charge voltage. When it was used with the battery fully charged, the 15KPA33CA's resistance was low enough to significantly draw current from the battery, depleting its charge and causing it to heat up quickly, seen in Figure 17. It was still able to suppress that transients, also shown in Figure 17, however it would clearly not be good to use the device if the battery has to be fully charged. This brings about the main limitation of TVS diodes in that it is desirable to have one that suppresses transients quickly enough but acts as an open circuit across the full desired operational range.

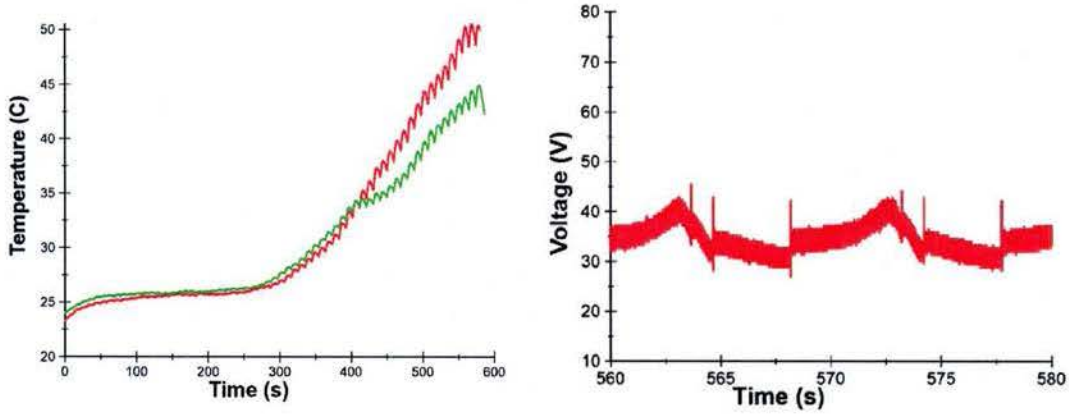

Figure 17: With the module nearly at peak charge the temperature started to increase drastically over long term use (left) the voltage suppression is identical to when the module was charged to its nominal voltage (right).

The next round of testing involved using 15KPA40CA with the 584 cm long cable. The setup is exactly the same as was previously documented with the only difference being the use of the 15KPA40CA diode in place the 15KPA33CA diode. The voltage of the bus, including the transients recorded, during three independent experiments are shown in Figure 18 along with the current measured through the device.

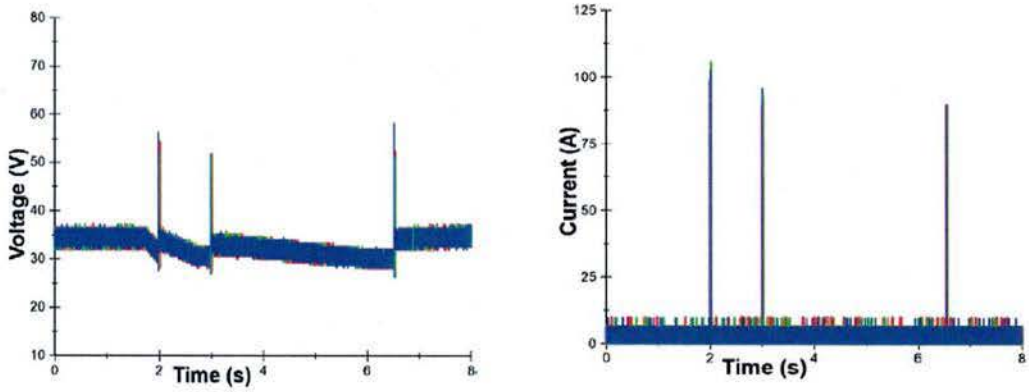

Figure 18: Transient voltage profile using the 15KPA40CA and the 230 in cables (left) the current shunted by the 15KPA40CA (right).

The 15KPA40CA was able to limit the voltage transients to roughly 55 V which is a little higher than the 15KPA33CA suppressed them to, as expected. This further demonstrates the tradeoffs of TVS diodes. Choosing one that is better matched for the desired operational voltage range comes at the cost of allowing transients to reach a slightly higher voltage. Since both diodes have roughly the same thermal constant, it is expected that they would heat up similarly when put through the same 60 cycle repetitive experiment. A photograph of the diode and a plot of its temperature during three identical 60 cycle tests can be seen in Figure 19. Figure 20 plots the diode's voltage and current profiles measured during two identical experiments using two different diodes. As shown there is a few volts of variation in the transient voltage reached but it remains for the most part consistent around 54 V.

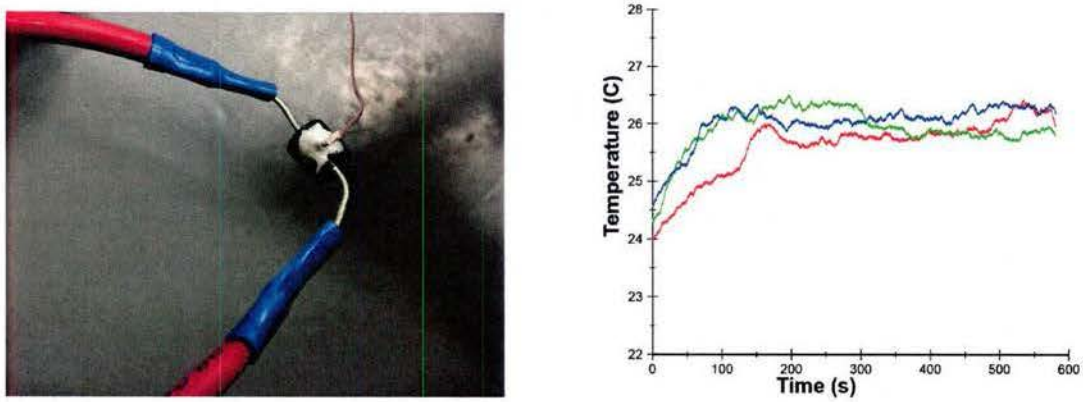

Figure 19: The 15KPA40CA with a T-type thermocouple thermal epoxied to the diode for temperature measurements (left) three tests showing the temperature rise of the TVS diode during the 60 cycle tests (right).

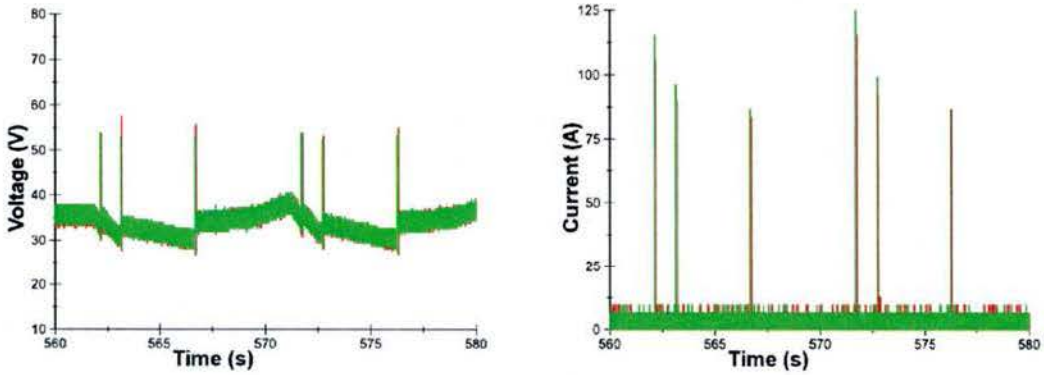

Figure 20: Transient voltages recorded (left) and current recorded through the 15KPA40CA diode (right) during the last few cycles of a repetitive experiment using two identical diodes in two different experiments to demonstrate consistency of the TVS diode.

IV.b. MOVs

MOVs were evaluated next. Table 2 displays the datasheet properties of a few of interest as taken from the LittleFuse website. Like TVS diodes, MOVs are offered in discrete increments of operational and clamping voltages. Through consultation with Littlefuse, an MOV that has a maximum continuous voltage that is 20% higher than the modules voltage is preferred. In the case of the 33 V module, the V20E35P appears to be the best choice. The other two MOVs shown in Table 2, the V07E30P and V10E23P, were also evaluated based off the full battery module voltage range and because simulation models of them were available from Littlefuse.

Table 2: The electrical characteristics for the MOVs used in this experiment, the V10E23P, V07E30P, and V20E35P.

Epoxy Coated Models		Phenolic Coated Models[2]		Size Disc Dia. (mm)	Max Continuous Voltage		Varistor Voltage at 1mA			Maximum Clamping Voltage		Max Peak Current (8 x 20µs 1 pulse)	Energy Rating (2ms, 1pulse)	Typical Capacitance f = 1MHz
Part Number (Base part)	Branding	Part Number (Base part)	Branding		$V_{M(AC)RMS}$	$V_{M(DC)}$	V_{NOM} Min	V_{NOM} Nom	V_{NOM} Max	V_C	I_{PK}	I_{TM}	W_{TM}	C
					(V)	(V)	(V)	(V)	(V)	(V)	(A)	(A)	(J)	(pF)
V10E23P	P10E23	V10P23P	P10P23	10	23	28	32.4	36.0	39.6	71	5	2000	12	3200
V07E30P	P7E30	V07P30P	P7P30	7	30	38	42.3	47.0	51.7	93	2.5	1000	7	1350
V20E35P	P20E35	V20P35P	P20P35	20	35	45	50.4	56.0	61.6	110	20	8000	115	10500

MOVs have three main characteristics that were considered when examining their specifications. These include the maximum continuous voltage ($V_{M(DC)}$), max clamping current (I_{PK}), and the maximum clamping voltage (V_C). Disk size is also a factor for MOVs as larger disk sizes come with an increased single transient event current I_{TM} and energy dissipation W_{TM} capability, respectively. Of those shown in Table 2, the lowest I_{TM} is 1000 A and the lowest W_{TM} is roughly 7 J, both of which are well above the ratings needed for transients expected here.

The MOVs were then tested in the same fashion as the TVS diodes were earlier. Each of the three MOVs were tested using both the 465 cm and 584 cm long cables, respectively. Figure 21 contains photographs of the three of the MOVs evaluated.

Figure 21: The V10E23P placed parallel to the bus with the differential voltage probes and the clamped-on current meter (left) the V07E30P with the same exact set up (middle) the V20E35P also with the same exact set up (right).

The first MOV evaluated was the V10E23P, whose 1 mA conduction current occurs when a voltage between 32.4 V and 39.6 V is applied. Its maximum clamping voltage is roughly 71 V, which is relatively high relative to many of the transients seen here. Remember that the 15KPA33CA TVS diode's maximum clamping voltage is listed at roughly 55 V. Figure 22 presents voltage and current data recorded during three independent experiments using the 465 cm long cable. Referring back to Figure 10, in which a plot of the voltages recorded with no current suppression applied, it should be noticed that the V10E23P appears to have little, if any effect on the voltage transients produced that are less than ~55 V. It does however suppress the higher ~75V transient down to roughly 55 V. Remember that the transients induced on the 465 cm long cable were suppressed to ~45 V when the 15KPA33CA TVS diode was used. This data suggests that the V10E23P is not effective solution for clamping the transients observed here. The data collected from the 584 cm long cable using the V10E23P is shown in Figure 23 where very similar results were obtained.

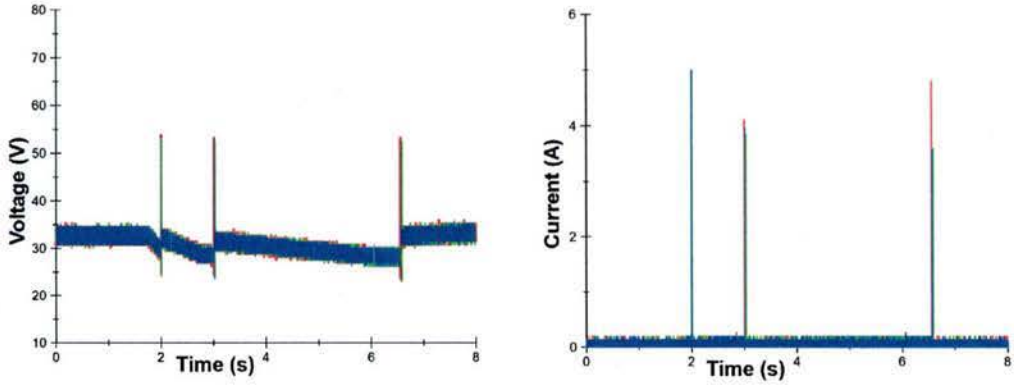

Figure 23: Transient voltage profiles measured during three tests performed using a 465 cm cable and a V10E23P MOV. Voltage (left) and MOV current (right) are shown.

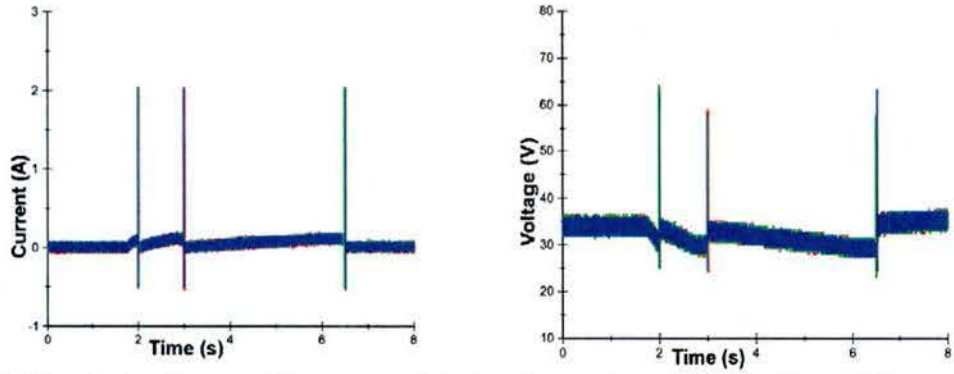

Figure 23: Transient voltage profiles measured during three tests performed using a 584 cm cable and a V10E23P MOV. Voltage (left) and MOV current (right) are shown.

From these results, it is clear that the better suppression should be obtained if an MOV with lower operational and maximum clamping voltage ratings is utilized. Since the V10E23P is already at the lower end of the battery's normal operating voltage range, one with lower ratings should conduct a significant current even in the idle state which would not be beneficial and therefore it was not evaluated. From Table 2, the other two devices listed V07E30P and the V20E35P respectively, each have higher nominal operating voltage and clamping voltage ratings than the V10E23P meaning that they are likely to be less effective. This hypothesis was confirmed with the data presented in Figures 24 through 27.

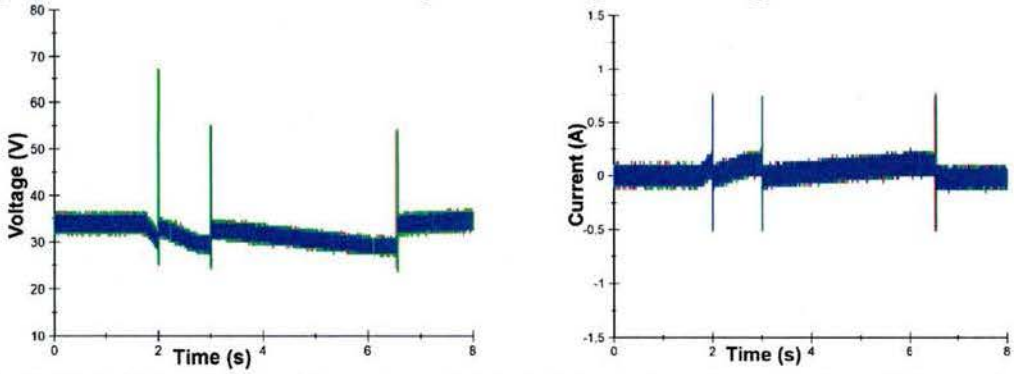

Figure 24: Transient voltage profiles measured during three tests performed using a 465 cm cable and a V07E30P MOV. Voltage (left) and MOV current (right) are shown.

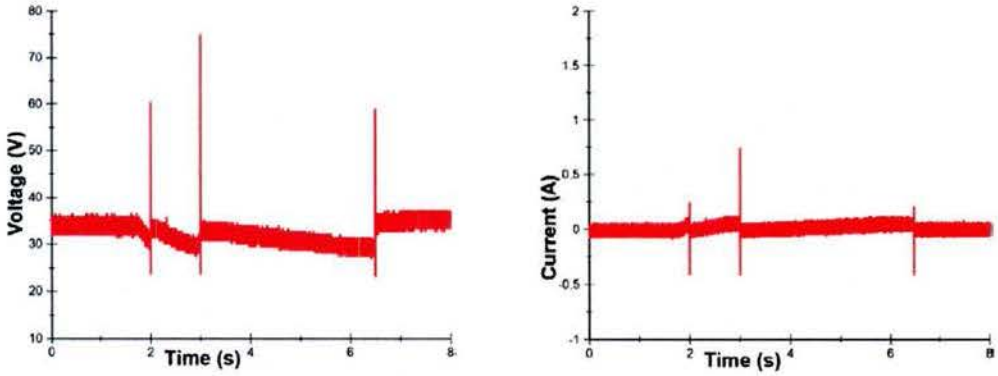

Figure 25: Transient voltage profiles measured during three tests performed using a 584 cm cable and a V07E30P MOV. Voltage (left) and MOV current (right) are shown.

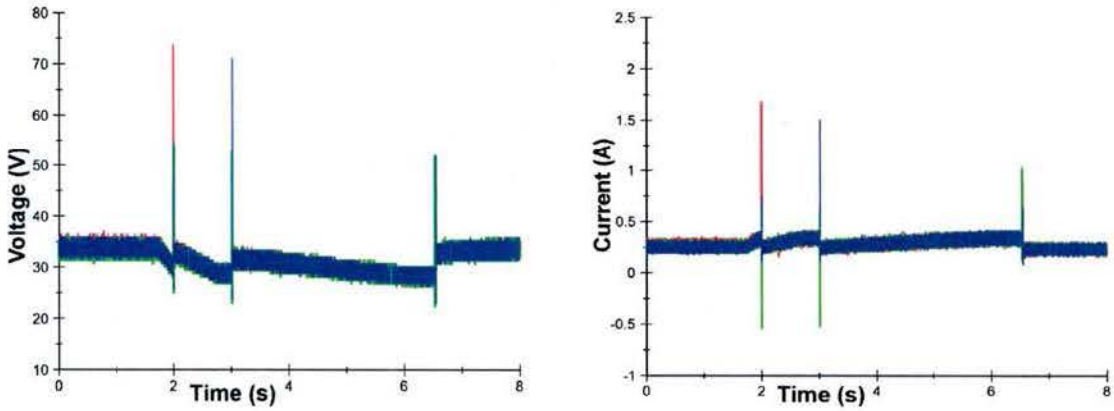

Figure 26: Transient voltage profiles measured during three tests performed using a 465 cm cable and a V20E35P MOV. Voltage (left) and MOV current (right) are shown.

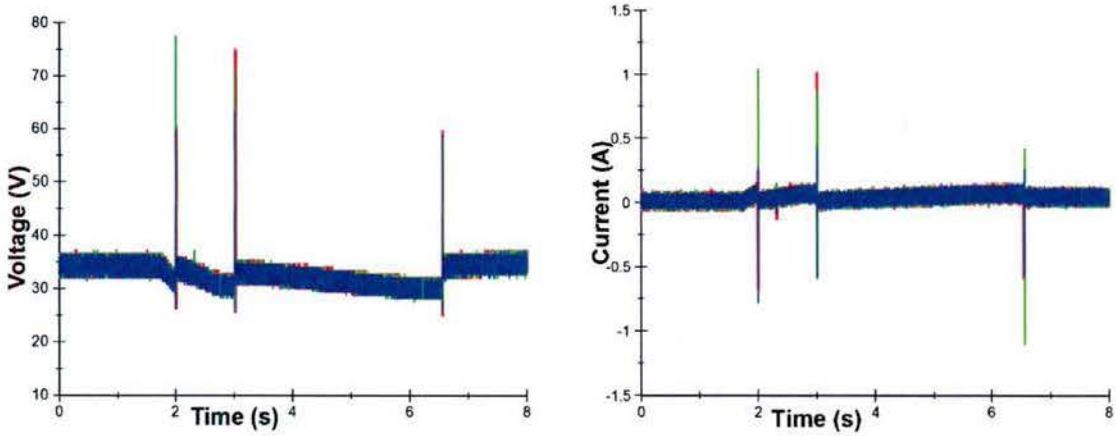

Figure 27: Transient voltage profiles measured during three tests performed using a 584 cm cable and a V20E35P MOV. Voltage (left) and MOV current (right) are shown.

Even though it did not perform all that well with the lower voltage transients, the V10E23P was still evaluated in a similar repetitive manner to the TVS diodes earlier to validate its repetitive effectiveness as well as its thermal response. A T-type thermocouple was affixed to the MOV using thermal epoxy and then it was subjected to the current profile of interest 60 consecutive times. A photograph of the epoxied thermocouple on the MOV along with a plot of the MOV's temperature during the experiment is shown in Figure 28. The voltage and current data, respectively, recorded during the last few cycles is shown in Figure 29 when the 465 cm long cable was used. As shown in Figure 23, the MOV does not do a good job of suppressing any of the transients except the higher ~75 V one that is occasionally seen. As expected, the MOV's temperature rises only slightly due to the lack of current conducted through it.

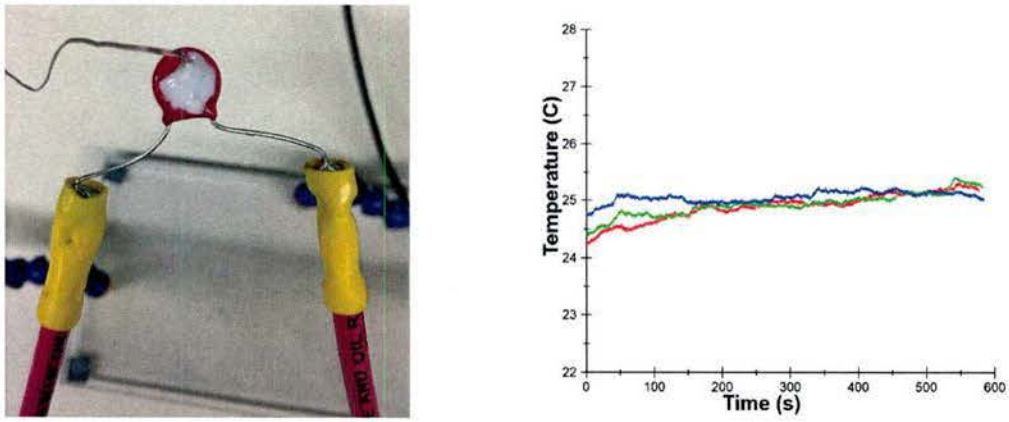

Figure 28: V10E23P with a T-type thermocouple attached using thermal epoxy for temperature measurements during the 60 cycle test (left) three temperature measurements of the V10E23P while clamping voltage transients during the 60 cycle tests (right).

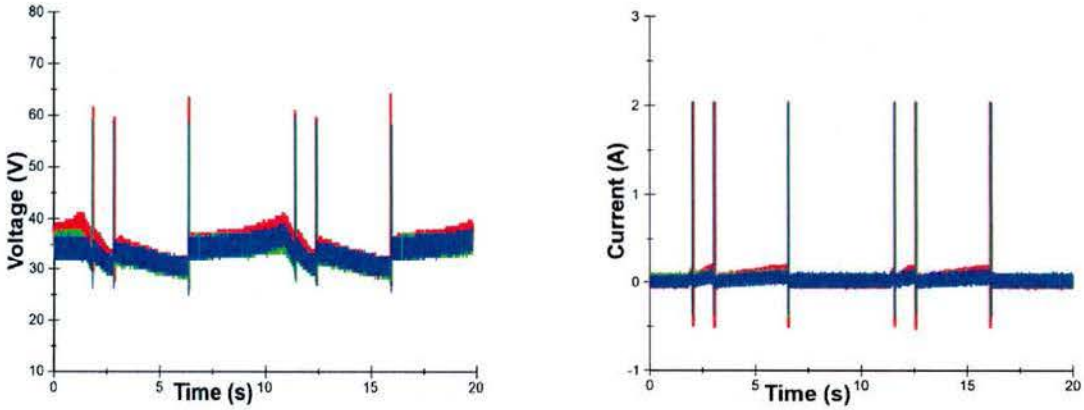

Figure 29: Transient voltage profiles of the last two cycles during the 60 cycle test (left) current shunted by the V10E23P corresponding to the transient voltage profiles (right).

The takeaway from this round of testing is that MOVs are likely not as effective in this application of suppressing transients as the TVS diodes were shown to be. Like TVS diodes, the MOVs only come in discrete voltage increments and the maximum clamping voltage is significantly higher than the nominal operational voltage range meaning that the voltage transients have to be quite significant in order to actually be suppressed.

IV.c. Active Circuit Topologies

As already highlighted, TVS diodes and MOVs each suffer from discrete voltage ranges they operate in. One possible solution to overcoming these limitations is to use actively controlled electronics to more accurately control when the suppression kicks in. A few different designs were conceived, simulated, and evaluated with mixed results. The first design is shown in Figure 30. The intent of the circuit is to redirect the transient energy through a shunt resistor (R7) when the bus voltage exceeds 39 V. The Zener diode (D7) is intended to enter revers breakdown when 39 V is applied. Once the transient reaches a voltage higher than 39 V, the gate-to-source voltage (V_{GS}), or the voltage across the pull-up resistor (R10), of the P-channel MOSFET is negative, with respect to the bus voltage, causing it to start conducting. The Zener diode (D8) is specified to enter reverse breakdown at 27 V. The voltage across the pull-down resistor (R9) is then

V_{TRAN} – 27 V then allowing the N-channel MOSFET (M5) to start conducting. R11 limits the current into the N-channel MOSFET. Once the N-channel MOSFET begins conducting, the transient voltage is applied across the low impedance power resistor (R7) intended to shunt away the stored inductive energy. Figure 31 presents simulation results in which the transients are well suppressed at just over 39 V. Figure 32 contains two photographs of the actual circuit evaluated on the experimental setup. The first is a close-up of the device soldered on a protoboard and the second is shows it installed within the test setup. Because there was concern that a MOSFET could fail and shunt the battery to ground through the low impedance power resistor permanently, a fuse as well as an electromechanical relay were placed in series with the power resistor as an extra precaution. Figure 33 contains the results recorded from the oscilloscope during the initial round of experimentation with this active design.

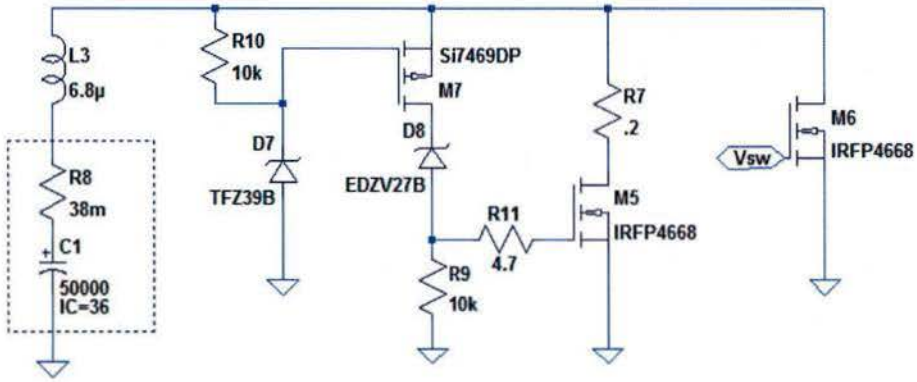

Figure 30: Circuit diagram of one active voltage transient suppression topology.

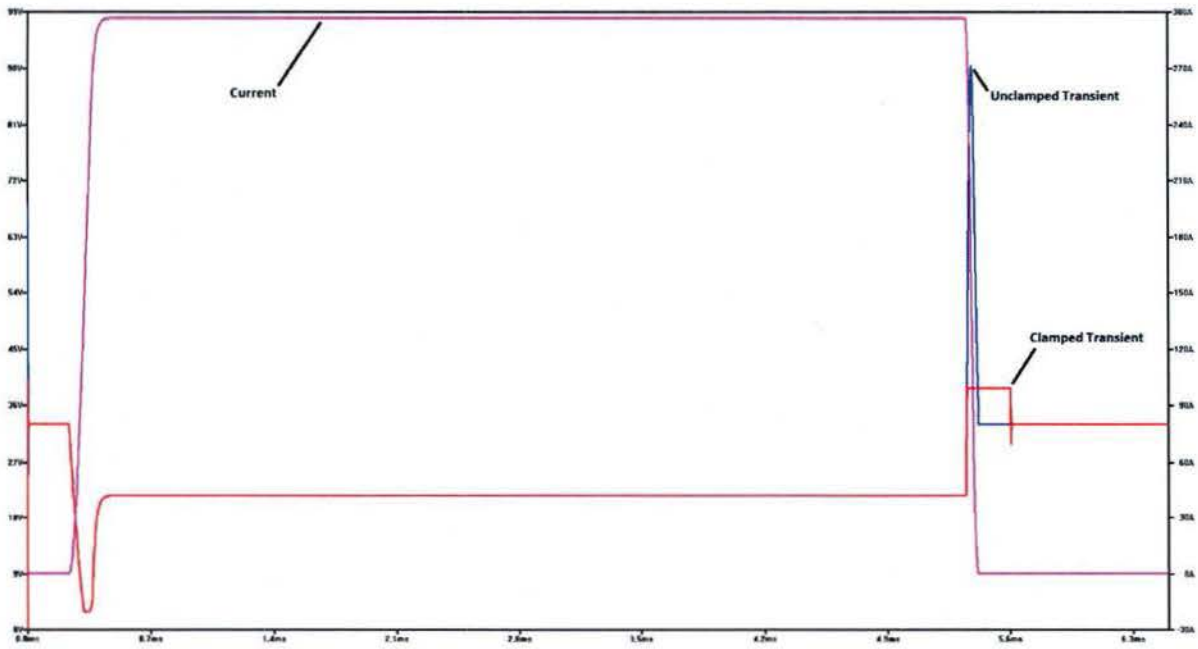

Figure 31: LTSPICE simulation results obtained from the active circuit topology shown in Figure 30.

Figure 32: Active voltage transient suppression device designed to mitigate voltage spikes. Photos of the protoboard circuit (left) and it installed within the experimental setup (right) are shown.

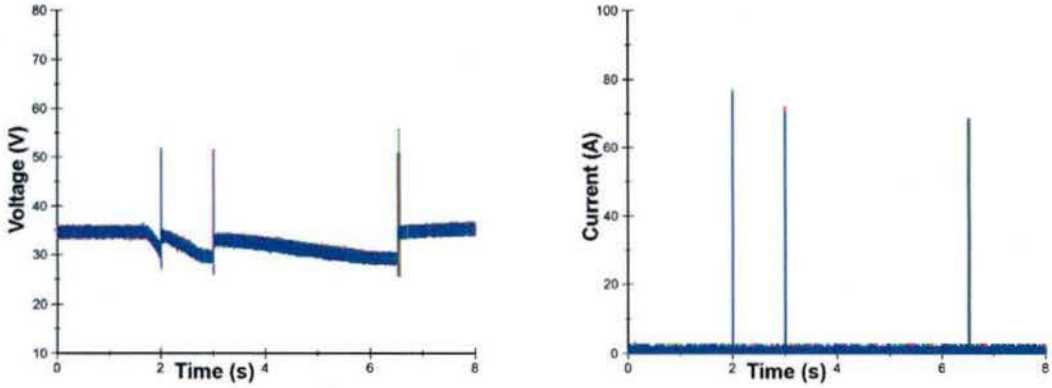

Figure 33: Voltage (left) and power resistor current (right) waveforms recorded from three experiments performed using the active suppression circuit shown in Figure 31.

Despite being designed to turn on at 39 V, the active transient suppression device appears to have clamped the voltage consistently at just over 50 V when the 584 cm long cable was used. Remember from Figure 10 that the unsuppressed voltage transients range anywhere from just over 60 V to nearly 80 V. The current shunted by the device is between 75 A and 80 A. It is somewhat unclear why the device does not do a better job of suppressing the transients at lower voltage. One speculation is that the turn on time of the MOSFETs is slow since there is no high current driver utilized in the circuit. This was done so as to minimize any additional power supplies needed to operate the circuit, keeping it passive. Attempts at using a resistance less than 0.2 Ω were made but each time, it conducted too much current causing its temperature to grow excessively and often times the MOSFET would also fail due to both thermal and likely transient voltages induced when the device turned off. In summary, this topology has promise but more work is needed to fully flush out the design and it is likely that additional driver hardware is needed.

One last active design was conceived and has only been partially evaluated to date, shown in Figure 34. This design utilizes a voltage comparator circuit to detect a transient event. The use of the comparator and a tunable reference voltage allows the turn-on voltage to be manually adjusted by the operator. When the bus voltage goes higher than the reference voltage, the comparator (U1) goes high, supplying current to the gate three MOSFETs connected in parallel. A 0.1 Ω shunt resistor is connected in series with the three

MOSFETs to suppress the transient energy. Three MOSFETs are used to distribute the transient energy and prevent them from overheating. Presently the device does a decent job of suppressing the transients however, because the driver opens and closes the gate quicker, new transients are formed within the circuit each time the suppression begins that causes the circuit to oscillate. The present plan is to add an RC circuit to the driver circuit that limits the turn on and turn off a little bit to prevent transients from occurring.

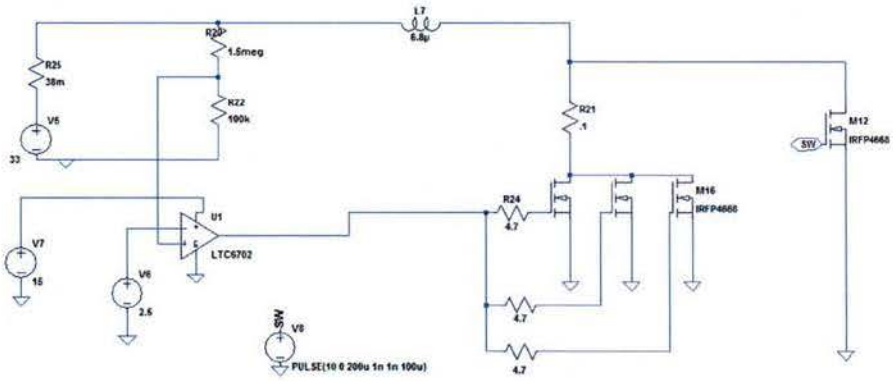

Figure 34: Schematic of the active transient suppression design using logic for a variable clamping voltage.

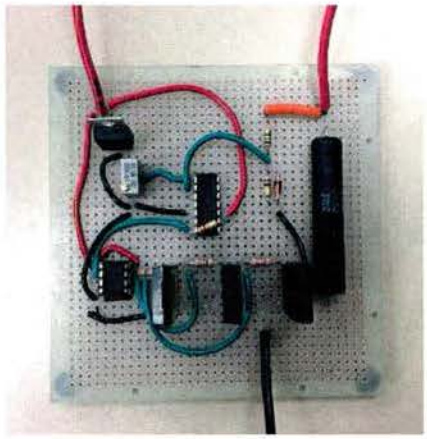

Figure 35: Photograph of the active transient suppression design shown in Figure 35 constructed on a protoboard.

V. Conclusion

It is clear from the data shown here that voltage transients should be of concern when electrochemical batteries are used to supply high rate intermittent currents to future Navy directed energy loads. The fast switching of the current and the large inductances present in long cable networks could induce significant voltage transients with quite a bit of energy that must be shunted away. If not shunted away, the voltages could be high enough to quickly damage other components within the electrical system, including the battery itself. Three different suppression techniques have been studied here, including TVS diodes, MOVs, and active electronic topologies. It was shown that TVS diodes and MOVs can be effective at shunting away voltage transients however they are offered in discrete voltage ranges that do not always line up with the voltages that need to be continuously applied and transients that need to be shunted. Both devices have a nonlinear *iv* curve with their resistance decreasing quickly above a certain point. Since the point at which

the resistance decreases rapidly needs to be greater than the nominal operating voltage, the device must allow for some transient to occur which may or may not be within the allowable tolerance of the system. Active topologies are more flexible but they are most likely larger in size, may require additional external hardware to function, and are not commercially available off the shelf.

The work performed here has highlighted the concerns that high voltage transients bring to a high voltage system and the need for some sort of suppression technology. TVS diodes appear to the most feasible solution but is possible that either the design of the battery will need to be somewhat flexible around the voltage of TVS diodes available if there is not one readily available or that closer coordination will have to occur with the TVS diode manufacturer in order to design a TVS diode with the right doping levels to meet the requirements of the system. More work is still needed to address the bugs in the active topologies evaluated here.

Task 2: Investigate the Dielectric Breakdown Strength of Vented Li-Ion Battery Electrolyte

I. Introduction

The US Navy is presently considering the use of electrochemical energy storage devices aboard their future fleet of vessels as both prime power and backup power generation sources [1-3]. Many different energy storage chemistries are being considered to meet a host of unique demands. Lithium-ion-batteries are among those with a great deal of promise due to their high combined power and energy density that allows them to be very versatile as both the source and sink of high power aboard a mobile platform. Lithium-ion batteries are available in many different chemistries and each offers its own advantages and disadvantages with respect to voltage, power density, energy density, impedance, and safety, respectively.

Battery failure often leads to thermal runaway, a process in which an increase in temperature changes the conditions in a way that causes a further increase in temperature [12]. Each of the different chemistries fails in a different way and has a different level of thermal runaway volatility. When a lithium-ion battery fails, the high temperature leads to an increase in pressure within the cell that causes an internal burst diaphragm to rupture in attempt to relieve pressure and prevent further thermal increase. Rupturing of the burst diaphragm releases internal gases, vented organic electrolyte compounds, to the surrounding environment. The chemical makeup of the vented gas is chemistry dependent with different levels of toxicity and flammability.

In most lithium ion batteries, the electrolyte solution consists of combinations of linear and cyclic alkyl carbonates including ethylene carbonate, dimethyl, diethyl, and ethyl-methyl carbonates (EC, DMC, DEC, and EMC) as well as electrolyte salts such as $LiPF_6$ or $LiClO_4$ [13]. Over a cell's useful lifetime, the electrolyte decomposes slowly, however when they are exposed to extreme voltage or temperature conditions, the electrolytes can react rapidly with the active electrode materials to release significant heat and gas [13, 14]. Thermal runaway begins as temperatures in excess of 200°C are reached, however breakdown of the solvents can occur slightly sooner. During these processes, many different gas products are produced, most of which are hydrocarbons with various levels of toxicity and flammability.

Among the chemistries being considered is lithium-iron-phosphate (LFP). The olivine LFP chemistry is safer than other layered or spinel battery chemistries but the increased safety comes with a reduced energy density in comparison with other chemistries. The Fe–P–O bond is stronger than the Co–O bond, so that when they are abused, the oxygen atoms are much harder to remove which reduces thermal runaway [12]. Venting of a lithium-ion cell occurs when a cell develops an internal short circuit, causing it to get too hot, when it is overcharged, causing the electrolytes own dielectric strength to be broken down, or when the cell simply gets too hot as a result of other external factors. Previous research, Figure 1, has shown that when the LFP chemistry vents, the gas released is made up primarily of carbon dioxide (CO_2), hydrogen (H_2), and ethene (C_2H_4), along with a few others in smaller proportions [13]. These proportions have been validated with in house research. How these gases affect the dielectric strength of a background gas is presently undocumented and must be studied as batteries become ready for deployment aboard future naval vessels.

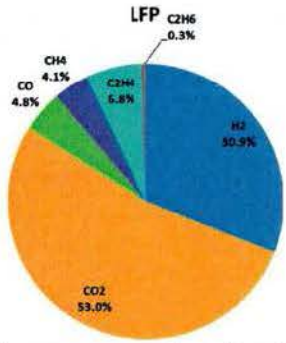

Figure 38: Detected components of produced gases (mol%) [13].

As already mentioned, lithium-ion batteries are being considered for use in a host of applications aboard future naval vessels and there is no one-size-fits-all solution. In some applications, batteries with open-circuit-potentials as high as 1 kV are being considered and voltage regulators will be used to adapt the voltage to that required by load. Though 1 kV is quite small compared to that of a medium voltage distribution system and most pulsed power systems, it is still significant and needs to be designed with caution. Electric field enhancements on the surfaces of the cells or conductors could amplify the electric field significantly and therefore dielectric breakdown under any possible scenario is something that should be studied in detail before batteries are deployed at the 1 kV level. Among these scenarios is the one where the ambient air condition is flooded with vented carbonates from a failed battery. The work being discussed here is aimed at studying this condition.

In 1889, Friedrich Paschen published what is now known as Paschen's Law in which the breakdown voltage between two electrodes is a function of the product of chamber pressure and the distance between the electrodes [17, 18]. The Paschen equation is written as

$$V_B = \frac{B \times pd}{\ln\left(\frac{A \times pd}{\ln\left(\frac{1}{\gamma}\right)}\right)} \tag{5}$$

where V_B is the gap breakdown voltage in V, A and B are gas dependent constants, γ is the secondary electron emission coefficient or the number of secondary electrons produced per incident positive ion, p is the gap pressure, and d is the distance between the two electrodes, respectively. Breakdown in a gas occurs as a result of free electrons colliding with neutral atoms as they accelerate from the cathode to the anode, due to the application of an electric field. At low pressure, the number of neutral ions present for ionization are low, decrasing the probability of streamer formation and breakdown occuring. At high pressures, the number of neutral ions is high, decreasing the ionization mean free path and the number of ions created, decreasing the liklihood for breakdown. The Pachen minimum defines the pressure-distance product, pd, that is optimum for breakdown to occur. Figure 2 plots the Pachen curve for a few different gases.

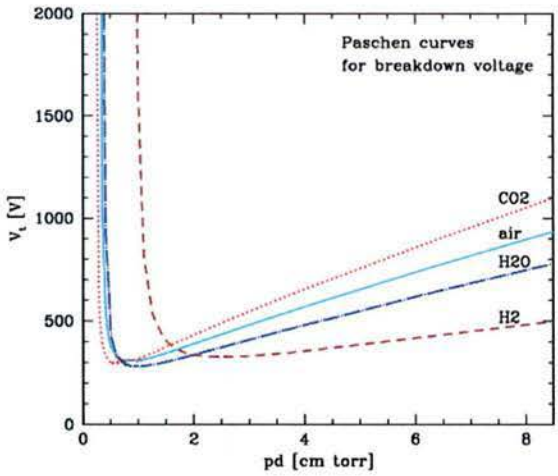

Figure 39: Paschen curves for five different gases [15].

In Figure 2, the respective Paschen curves for air, H_2, and CO_2, are all plotted. For a given pd product in the linear region, CO_2 has the highest breakdown voltage while H_2 has the lowest [16, 19, 20]. Since vented LFP electrolyte is almost entirely CO_2 and H_2, it could be hypothesized that its Paschen curve will resemble that of air. Speculation could be made that the breakdown potential may be slightly higher than that of air given that CO_2 is in slightly higher volume than H_2, however the other smaller gas players are

unknown contributors, making it critical that the breakdown potential be empirically studied. The work presented here will only investigate the impact the vented gas has on the ambient pressure condition, though ultimately, its impact across a full pressure range is of interest. As will be shown later, the pd products studied here range between 5 cm*torr and 35 cm*torr, placing them in the linear region shown Figure 2.

II. Experimental Setup

The work performed here is aimed at studying the dielectric strength of an air environment that is flooded with gas from a vented LFP battery. The experimental setup is shown graphically in Figures 2 through 6, respectively. Figure 2 presents a schematic diagram of the entire test setup and Figure 3 shows the entire setup photographically. Figures 4, 5, and 6 each presents a different respective subsection in greater detail.

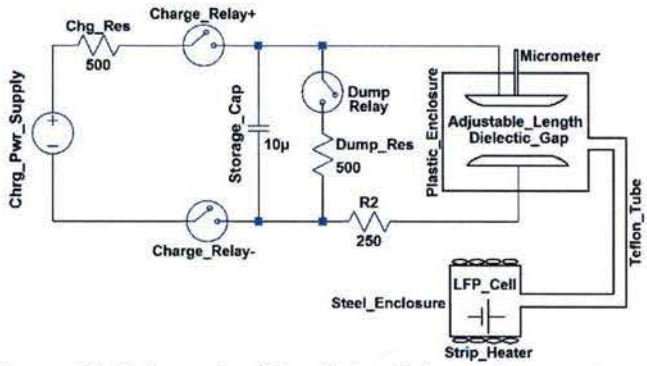

Figure 40: Schematic of the dielectric breakdown test setup.

As shown in Figures 2 and 3, respectively, a charging power supply is used to charge up a 10 µF capacitor to potentials as high as 4 kV. The capacitor acts as an intermediate energy storage device that limits the energy dissipated in an arc across the dielectric gap. Current limiting resistors are used both when charging the capacitor and to limit the current through the gap during discharge. Isolation relays are used to take the charging power supply out of the circuit prior to discharge. The charge and dump portion of the circuit is shown photographically in Figure 4. The dielectric gap is housed within an acrylic chamber that is shown in Figure 5.

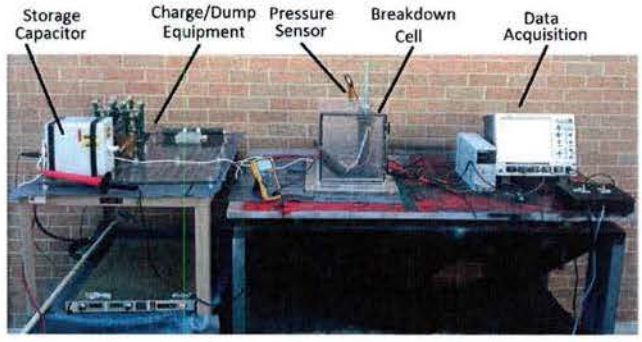

Figure 41: Photograph of the entire dielectric breakdown test setup.

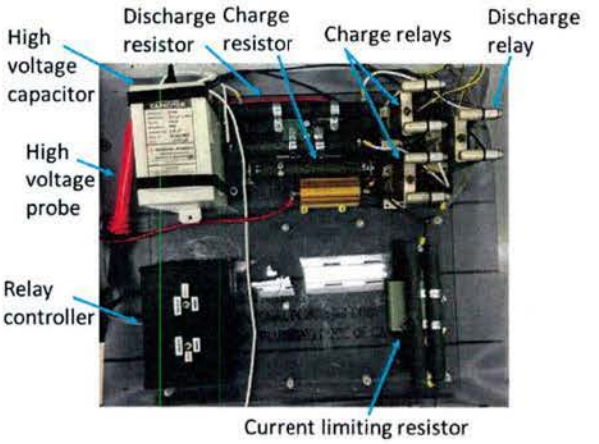

Figure 42: Photograph of the UTA dielectric breakdown experimental circuit setup.

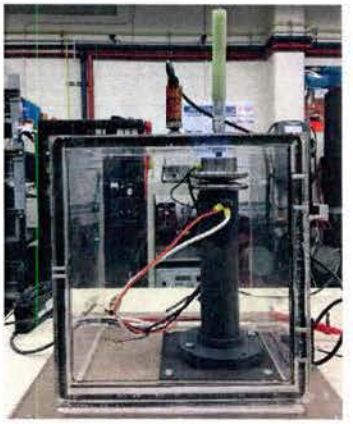

Figure 43: Sealed acrylic chamber containing electrodes used to induce voltage breakdown.

As presently configured, the chamber is not sealed to hold a constant applied pressure or vacuum. A pressure sensor is mounted on the top of the chamber for measurement of the chamber's bulk pressure during experimentation. The gap is fabricated of two 4340 steel electrodes machined with a Bruce profile [16] to ensure uniform dielectric field across the gap. The uniformity of the gap separation is ensured using Pressurex® film prior to experiments being performed. The upper electrode is mounted to a micrometer that has accuracy to ± 0.00015 in so that the gap separation can be adjusted accurately. A G-10 insulator is used to prevent human contact with the micrometer while the gap is charged up while allowing for adjustment. High temperature Teflon tubing is used to pipe gas from the vented LFP cell, discussed next, into the chamber. The lower electrode is fixed and mounted to a PVC stand that is affixed to the lower wall of the chamber.

Cylindrical lithium ion cells of the 26650 form factor and the $LiFePO_4$ chemistry are being used in the experiments documented here. Individual cells are failed in a controlled manner and the vented gas is piped into the acrylic chamber using the Teflon tubing discussed earlier. To fail the cells, they are enclosed in a 31.75 mm diameter steel tube that is capped at one end and vented to the other end using a brass barb fitting. The cell is placed within the tube and outer perimeter of the tube is wrapped with 220 VAC, 1 kW, resistive heat tape. The heat tape is used to heat up the steel and subsequently the cell within it. Once temperatures in excess of 200°C are reached, the cell's pressure cap bursts and the vented

carbonates are piped out into the chamber. A photograph of the steel tube wrapped in heat tape is shown photographically in Figure 6.

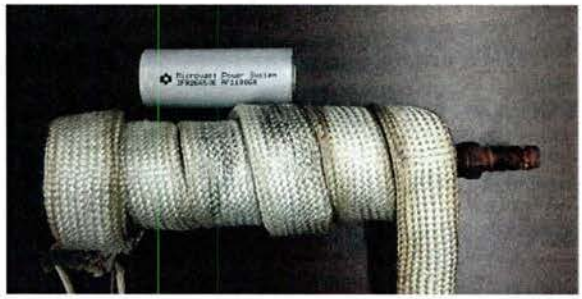

Figure 44: Pipe housing, heat tape, and LiFePO4 cell setup used to direct vented gas into the acrylic test chamber.

During an experiment, a cell is vented and the chamber is filled with vented gas. It should be noted that a small brushless DC fan, not shown in Figure 4, is placed on the lower wall of the test chamber to provide gas circulation with minimal disruption. Once gas begins to pipe in, the capacitor is charged up to the desired charge voltage and isolated from the charging supply. The gap is then adjusted closer together until breakdown occurs. Data is saved, the gap is expanded quickly, and the charge/breakdown process is repeated while the chamber is still filled with gas. Typically four to six measurements are able to be made using the gas from a single cell. Multiple cells have been vented so that a statistically relevant sample size is obtained.

While being charged, the capacitor's voltage is measured using a 40 kV Fluke high voltage probe connected to a Fluke millimeter. During a breakdown experiment, the gap voltage is measured using a LeCroy PPE4kV high voltage probe with a bandwidth of 400 MHz. The gap discharge current is measured using a LeCroy CP150 with a bandwidth of 10 MHz. Pressure is monitored using a Omega PX309 sensor that is able to measure up to 345 kPa with 0.25% accuracy. All of these measurements are collected using a LeCeroy WaveSurfer oscilloscope.

III. Experimental Results

Four different sets of experiments will be reported here. In the first, the applied gap voltage was varied between 0.5 kV and 2.5 kV, with increments of 0.1 kV, in an ambient air environment and the gap distance at which breakdown occurs with each respective applied potential was recorded. This data was collected to establish a baseline of the breakdown voltage vs *pd* for the experimental setup being used and for comparison against similar data published in the open literature. The data that was collected will be presented two ways, in Figures 7 and 8 respectively. In Figure 7, the breakdown voltage is plotted as a function of the gap distance at which the breakdown occurred. Error bars represent the standard deviation recorded among the five measurements recorded with each applied voltage. As shown, the data is quite repeatable with few outliers observed. Figure 8 plots the breakdown voltage as a function of pd where d is the same gap distance plotted in Figure 7. Since the pressure did not vary significantly over the experiments performed, the two plots look nearly identical as expected. The gap distances recorded were used in Paschen's voltage breakdown equation, equation 1, to determine their accuracy. Figure 8 shows a comparison of the data recorded and the breakdown voltage calculated using the respective recorded distances, illustrating the accuracy of the data recorded.

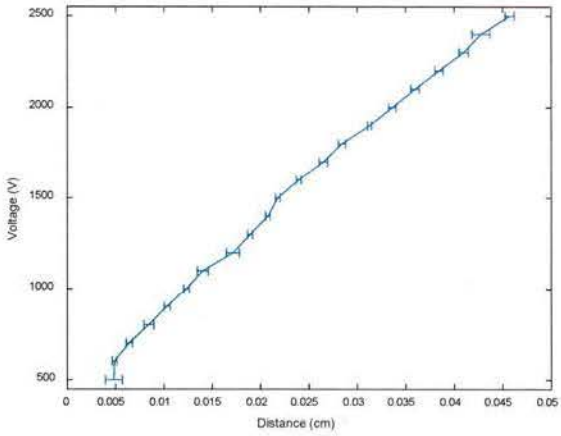

Figure 45: Breakdown votlage as a function of average gap distance. Error bars represent the standard deviation recorded over five measurements with each applied voltage.

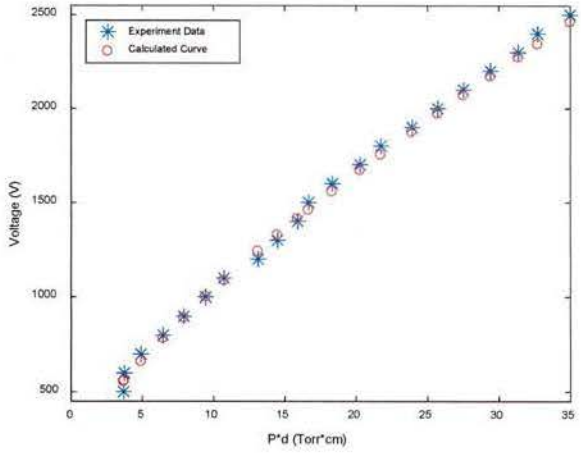

Figure 46: Breakdown voltage plotted as a function of the product of chamber pressure and breakdown gap distance, for both experimental and calculated data.

The next three sets of experiments are those collected when vented electrolyte filled the chamber using the procedure discussed earlier. Each series of experiments are identical with the only difference being the applied voltage. A 1 kV lithium-ion battery will have an open circuit potential around 1 kV but a conduction voltage that varies between roughly 0.75k V and 1 kV. Though there is no reason that the potential should go over 1 kV, voltages of 0.75 kV, 1 kV, and 1.25 kV respectively, were chosen for evaluation here. In each series of experiments, three LFP lithium-ion cells were vented and as many measurements as could be recorded with each were made. The data presented with an applied voltage of 0.75 kV, 1.0 kV, 1.25 kV are plotted in Figures 9, 10, and 11 respectively.

In each of the three plots, similar trends are observed with the gap distances being slightly wider, between 10% and 20% on average, when vented electrolyte is present in the chamber. Though there is some variation within the measurements, there are no significant outliers that would bring any uncertainty to the data. When evaluating the results, it is important to remember the discussion earlier about the breakdown potentials of CO_2, H_2, and air for a given *pd* product. The hypothesis discussed earlier appears to be verified that the breakdown potential is slightly higher than that of air due to the high CO_2 volume

but that it may be slightly reduced from that expected of CO_2 due to the presence of H_2 and other smaller volume chemical contents. What is verified here is that the presence of H_2 and the other contents does not dramatically impact the breakdown potential meaning that in the design of a high voltage battery, it is likely sufficient to design dielectric gaps assuming an air dielectric with the appropriate safety factors accounted for.

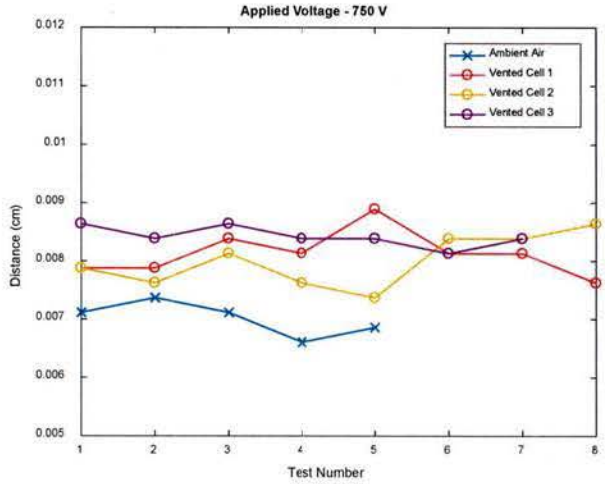

Figure 47: Breakdown distance measured multiple times from three identical vented LFP cells as well as ambient air, respectively, with an applied gap potential of 0.75 kV.

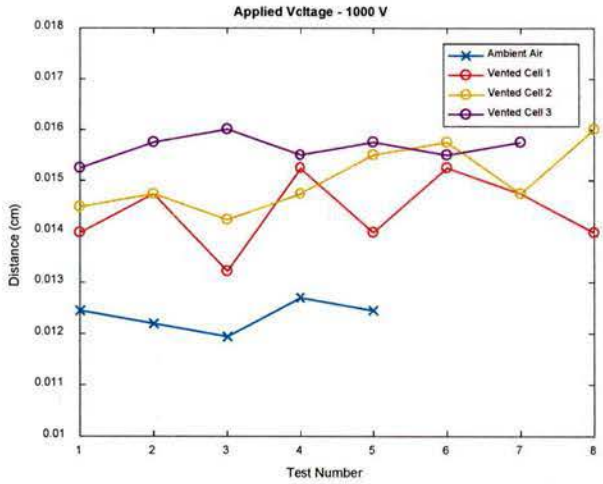

Figure 48: Breakdown distance measured multiple times from three identical vented LFP cells as well as ambient air, respectively, with an applied gap potential of 1.0 kV.

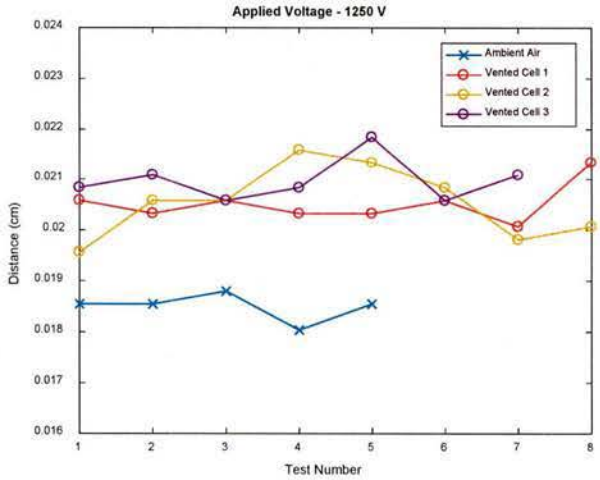

Figure 49: Breakdown distance measured multiple times from three identical vented LFP cells as well as ambient air, respectively, with an applied gap potential of 1.25 kV.

IV. Conclusion

The results from ambient air testing proves to be relatively linear over the voltage range tested, meaning that the curve plotted in Figure 9 is part of the linear section of the Paschen curve. Also according to Figure 8 the standard deviation for each voltage is low, the largest being $\pm$.001 cm, proving that the breakdown electrode gap distance does not vary much during testing. With the preliminary, ambient air, testing complete and verified to be accurate the testing then involved venting the LFP gases into the chamber to determine its effect on dielectric strength.

The three voltages investigated are 750 V, 1000 V, and 1250 V, as seen in Figures 10-12. According to the data the LFP gases did in fact have an effect on the dielectric strength of the test chamber environment. For all three voltages the breakdown electrode gap distance increased in the presence of the vented gases. The breakdown distance increase due to the vented LFP gases ranged anywhere from .001 - .003 cm, meaning the gases vented into the test chamber increased the dielectric strength by a small amount. The results prove promising for storage purposes, so that the specified clearance or method of storage in ambient air conditions will not cause problems in the event of battery failure and the presence of vented LFP gases.

References

[1] J. Thongam, et al. "All-electric ships—A review of the present state of the art," 8th International Conference and Exhibition on Ecological Vehicles and Renewable Energies, pp. 1-8, March 2013

[2] Next Generation Integrated Power System, NGIPS Technology Development Roadmap, Ser 05D / 349, November 30, 2007.

[3] D.A. Wetz, P.M. Novak, B. Shrestha, J.M. Heinzel, and S.T. Donahue, 'Electrochemical Energy Storage Devices in Pulsed Power,' IEEE Transactions on Plasma Science, Vol. 42, No. 10, Part 2, pp. 3034 – 3042, October, 2014.

[4] D.A. Wetz, B. Shrestha, and P.M. Novak, 'Pulsed Evaluation of High Power Electrochemical Energy Storage Devices,' IEEE Transactions on Dielectrics and Electrical Insulation, Vol. 20, No. 4, pp. 1040 – 1048, August, 2013.

[5] Cohen, I.J.; Wetz, D.A.; Kelley, J.P.; Heinzel, J.; Donahue, S., "Evaluation of a high rate hybrid energy storage module (HESM)," Electromagnetic Launch Technology (EML), 2014 17th International Symposium on , vol., no., pp.1,7, 7-11 July 2014

[6] Office of Naval Research. "Hybrid Energy Storage Module (HESM): Amendment 001" 13-SN-0007 [Online]. Available: http://www.onr.navy.mil/~/media/Files/Funding-Announcements/Special-Notice/2013/13-SN-0007-Amendment-0001.ashx. [Accessed 10 Dec 2013]

[7] "Copper Wire Resistance and Inductance Calculator", *Ampbooks.com*, 2017. [Online]. Available: https://ampbooks.com/home/amplifier-calculators/wire-inductance/. [Accessed: 21- May- 2017].

[8] "What is Transient Voltage? - Electronic Products", *Electronicproducts.com*, 2017. [Online]. Available: http://www.electronicproducts.com/Passive_Components/Circuit_Protection/What_is_Transient_Voltage.aspx?id=2780. [Accessed: 02- Jun- 2017].

[9] "What are TVS diodes", *SEMTECH.com*, 2017. [Online]. Available: http://www.semtech.com/images/promo/What_are_TVS_Diodes.pdf. [Accessed: 05- Apr- 2017].

[10] "Varistor | Metal Oxide Varistor - Littelfuse", *Littelfuse.com*, 2017. [Online]. Available: http://www.littelfuse.com/products/varistors.aspx. [Accessed: 13- Feb- 2017].

[11] "Truth About MOVs - Zero Surge", *Zero Surge*, 2017. [Online]. Available: https://zerosurge.com/truth-about-movs. [Accessed: 05- Feb- 2017].

[12] "Lithium iron phosphate battery", *En.wikipedia.org*, 2017. [Online]. Available: https://en.wikipedia.org/wiki/Lithium_iron_phosphate_battery. [Accessed: 19- May- 2017].

[13] A. Golubkov, D. Fuchs, J. Wagner, H. Wiltsche, C. Stangl, G. Fauler, G. Voitic, A. Thaler and V. Hacker, "Thermal-runaway experiments on consumer Li-ion batteries with metal-oxide and olivin-type cathodes", RSC Adv., vol. 4, no. 7, pp. 3633-3642, 2014.

[14] E. Roth and C. Orendorff, "How Electrolytes Influence Battery Safety", *Interface magazine*, vol. 21, no. 2, pp. 45-49, 2012.

[15] C. Helling, M. Jardine, C. Stark and D. Diver, "Ionization in Atmospheres of Brown Dwarfs And Extrasolar Planets. III. Breakdown Conditions for Mineral Clouds", *The Astrophysical Journal*, vol. 767, no. 2, p. 136, 2013.

[16] High-voltage engineering, 1st ed. New Delhi: M. S. Naidu, V. Kamaraju, p. 234.

[17] L. Berzak, S. Dorfman and S. Smith, "Paschen's Law in Air and Noble Gases", p. 1, 2006.

[18] Friedrich Paschen (1889). "Ueber die zum Funkenübergang in Luft, Wasserstoff und Kohlensäure bei verschiedenen Drucken erforderliche Potentialdifferenz (On the potential difference required for spark initiation in air, hydrogen, and carbon dioxide at different pressures)". Annalen der Physik. 273 (5): 69–75

[19] "Gaseous Breakdown & Paschen's Law", *Home.earthlink.net*, 2017. [Online]. Available: http://home.earthlink.net/~jimlux/hv/paschen.htm. [Accessed: 18- May- 2017].

[20] "Electrostatics and Surface Physics Laboratory", *Physics.ksc.nasa.gov*, 2017. [Online]. Available: https://physics.ksc.nasa.gov/CurrentResearch/Breakdown/Breakdown.htm. [Accessed: 19- May- 2017].